The Long-Wave Infrared Earth Image as a Pointing Reference for Deep-Space Optical Communications

A. Biswas,[1] S. Piazzolla,[1] G. Peterson,[2] G. G. Ortiz,[1] and H. Hemmati[1]

Optical communications from space require an absolute pointing reference. Whereas at near-Earth and even planetary distances out to Mars and Jupiter a laser beacon transmitted from Earth can serve as such a pointing reference, for farther distances extending to the outer reaches of the solar system, the means for meeting this requirement remains an open issue. We discuss in this article the prospects and consequences of utilizing the Earth image sensed in the long-wave infrared (LWIR) spectral band as a beacon to satisfy the absolute pointing requirements. We have used data from satellite-based thermal measurements of Earth to synthesize images at various ranges and have shown the centroiding accuracies that can be achieved with prospective LWIR image sensing arrays. The nonuniform emissivity of Earth causes a mispointing bias error term that exceeds a provisional pointing budget allocation when using simple centroiding algorithms. Other issues related to implementing thermal imaging of Earth from deep space for the purposes of providing a pointing reference are also reported.

I. Introduction

The potential for order-of-magnitude enhancement in deep-space communications capacity, while simultaneously reducing spacecraft burden [1], using lasers, requires submicroradian beam-pointing accuracy. For reasonable distances out to Mars or even Jupiter, transmitting a beacon laser from Earth to serve as an absolute pointing reference has been considered viable; however, for the outer reaches of the solar system, an alternative to using such a beacon would be of great benefit. In this article, we will present the prospects and consequences of a concept based on using the Earth image sensed in the thermal infrared [2,3] spectral region as a pointing reference.

Future laser-communication systems deployed on deep-space platforms will use near-diffraction-limited optical transceivers with aperture diameters ranging from 30 to 80 cm. With these systems, high peak-to-average-power laser transmitters received by photon-counting receivers on the ground (Earth) will result in the best photon efficiency (bits/photon). State-of-the-art lasers that satisfy the high peak-to-average-power ratio, coupled with the availability of efficient detectors, force the operating wavelength for

[1] Communications Architectures and Research Section.

[2] Breault Research Organization, Tucson, Arizona.

The research described in this publication was carried out by the Jet Propulsion Laboratory, California Institute of Technology, under a contract with the National Aeronautics and Space Administration.

deep-space optical links to be at discrete values in the near-infrared spectral region of 1 to 1.55 μm. Transmitting high-rate data from deep space back to Earth at these wavelengths requires (1) an absolute pointing reference; (2) accurate computation of point-ahead angles; and (3) line-of-sight stabilization against host platform disturbance. For distances spanning Mars and Jupiter ranges, preliminary designs [4,5] that meet these requirements have been based upon a combination of (1) receiving and processing the signal from an Earth-transmitted laser beacon; (2) processing of the Earth image sensed in the visible or near-infrared spectral regions; (3) using onboard inertial reference for line-of-sight stabilization; and (4) using passive isolation for rejecting higher-frequency disturbances from the platform. On the other hand, from near-Earth space platforms out to lunar distances, a laser beacon transmitted from Earth can be sufficiently bright to satisfy all the pointing, tracking, and line-of-sight stabilization requirements. As distances increase beyond Jupiter, transmitting a ground-based laser beacon to serve as an absolute pointing reference becomes increasingly difficult. Degradation of the laser beam due to atmospheric turbulence is a key contributing factor, although adaptive optical techniques for mitigating this degradation cannot be ruled out. Other difficulties with transmission of high-power lasers to outer planets arise due to unscheduled interruptions, caused either by cloud blockage or regulatory agency restrictions. Given these difficulties, absolute pointing schemes that do not require a laser beacon transmitted from Earth are highly desirable and will ease the future implementation of laser communications.

Two alternative schemes have been identified to-date, one based upon the use of high-accuracy star trackers [6] and the second using the Earth image viewed in the long-wave infrared (LWIR) spectral band (8 to 13 μm). The latter approach is the topic of this article.

LWIR imaging was motivated by the observation that Earth emission can be sensed from anywhere within the solar system and is not plagued by phase effects encountered with "viewing" Earth using reflected sunlight. Figure 1 shows visible (left) and LWIR (right) images of Earth. The LWIR image was taken by the Thermal Emission Imaging System (THEMIS) instrument onboard the Mars Odyssey spacecraft on April 21, 2001, during its cruise to Mars. Here the phase effects that plague visible imaging are emphasized relative to an LWIR-sensed image. The expected emissivity variations of approximately 6:1 in the LWIR also will be smaller than albedo variations of 10,000:1 in the visible and near-infrared spectral bands.

The outline of the remainder of this article will be as follows. In Section II, a conceptual reference design of an optical transceiver along with some operational assumptions will be described. In Section III, radiometric estimates will be presented in order to calculate the LWIR Earth signal and accompanying background photon fluxes arriving at the focal plane of an optical transceiver. In Section IV, our approach toward quantifying the emission nonuniformity of Earth and its effect on the centroiding of the Earth image will be presented. Section V will conclude the discussion, summarizing the prospects and consequences of utilizing an Earth thermal image pointing reference.

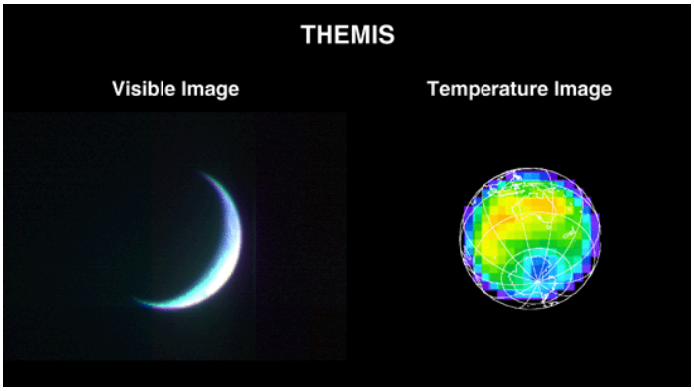

Fig. 1. Visible Earth image versus thermal image.

II. Reference Design of Optical Transceiver

Figure 2 shows a conceptual reference design for an optical transceiver that would use the Earth thermal image as an absolute pointing reference. The optical transceiver comprises an afocal telescope with a fast steering mirror (FSM) at a reimaged pupil. A solar rejection filter is used to prevent direct solar illumination while also rejecting entry of out-of-band solar and Earth-image light. This filter will have high transmission at the LWIR (8 to 13 μm) and transmit/receive laser bands in the visible/near-infrared (VIS/NIR) (1.00 to 1.55 μm), with good blocking characteristics outside these bands. We have not identified the substrate or coatings for such an optical element with these properties yet. The incoming light path following the FSM is split into LWIR and VIS/NIR paths with a beam splitter (BS), designated BS1 in Fig. 2. Again we assume that such a beam splitter exists with desirable optical quality and reflection/transmission characteristics at the VIS/NIR and LWIR wavelengths.

Earth emission collected by the telescope and incident upon the infrared acquisition and tracking detector will be accompanied by additive stray LWIR photons from the Sun and background from internally generated emission from optics along the receiving path. These are shown by the red and yellow arrows in Fig. 2. Lens 1 focuses the Earth emission on the focal plane. A narrow-bandpass filter (NBF), designated NBF1, that optionally can be used to further spectrally filter the Earth emission incident on the focal plane, is shown. The VIS/NIR light from the Earth and Sun that is transmitted through the VIS/NIR passband of the solar rejection filter is transmitted through BS1 and BS2 (green arrows). An internal inertial reference source similar to the magneto-hydrodynamic inertial reference unit (MIRU) [4] that was developed for the Mars Laser Terminal (MLT) is assumed to generate a reference laser beam, also in the VIS/NIR but spectrally separated from the transmitter and uplink laser light (dark green arrow in Fig. 2). At beam splitter 3 (BS3), the inertial reference unit laser and uplink laser are spectrally split and, along with some fraction of the VIS/NIR background from the Earth and Sun, are directed toward detectors labeled D2 (receive detector) and D3 (line-of-sight stabilization detector) in Fig. 2. Thus, D2 receives

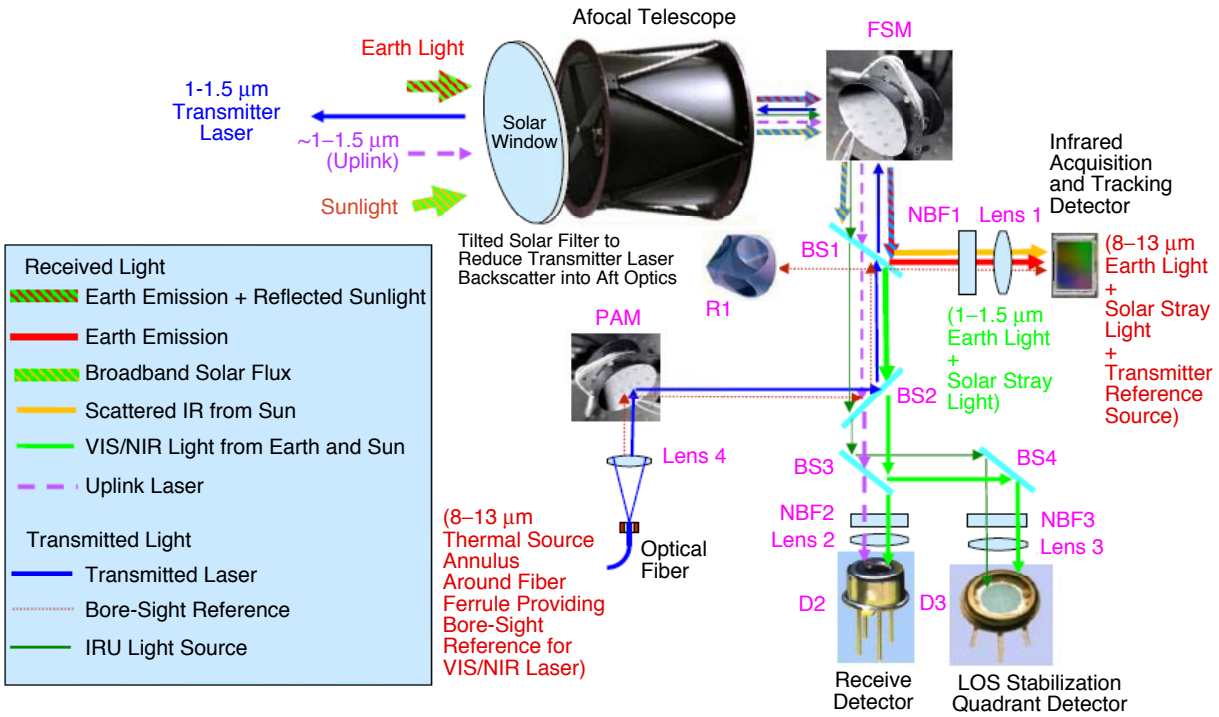

Fig. 2. Conceptual reference design for an optical transceiver that will use the Earth thermal image as an absolute pointing reference.

the uplink laser, and the resulting signal is processed to extract information that may be transmitted on an optical uplink. D3 serves as a part of the line-of-sight stabilization control loop, as described for the MLT. Note that finer spectral filtering than allowed by the solar rejection filter is implemented by means of the narrow-bandpass filters shown in Fig. 2 as NBF2 and NBF3.

The transmitted laser light is optically coupled to the transceiver through a fiber. After collimating the fiber input, the NIR laser transmitter beam is reflected off a point-ahead mirror (PAM) and folded (BS2) into the main transmit/receive path so that after transmission through BS1 the laser beam can be coupled out of the telescope (blue line in Fig. 2) while maintaining the ability to steer the beam with the FSM. To maintain reference with the transmitted laser on the LWIR acquisition and tracking sensor, a LWIR source bore-sighted to the NIR laser light co-propagates with the laser beam until it undergoes multiple reflections from BS1 and the retroreflector (R1 in Fig. 2) prior to being brought to incidence on the LWIR focal plane (brown dotted line in Fig. 2).

The reference optical transceiver design will use the image of Earth for acquisition and as an absolute pointing reference, whereas the line-of-sight stabilization against vibrational disturbances from the platform that is not rejected by passive isolation will be rejected through the use of an inertial reference unit, not shown in Fig. 2. Conceptually, this scheme can be used to communicate from any range within the solar system without requiring a co-operative laser beacon to be transmitted from Earth. In other words, if there were no laser uplink, the transceiver would be able to downlink data to a ground-based receiver on Earth. For the present discussion, the optical reference design is assumed to be ideal and diffraction limited at both VIS/NIR and LWIR wavelengths.

The Earth image size sensed in the LWIR from space will decrease with distance until the diffraction limit is reached. A simplified view of the pointing problem is gained by comparing the Earth image size with the transmitted laser beam width with the idealized diffraction-limited assumption mentioned above. It is reasonable to assume that optical transceiver diameters will increase as the distance from which communications are required increases. The Earth image sensed in the LWIR decreases with distance until it reaches a fixed size that is limited by diffraction. Using 10-μm to represent the LWIR band and 1.064 μm for the transmitted laser wavelength, the diffraction-limited Earth angular image size is 10 to 20 times the transmitted angular beam width, for distances greater than 2 AU and optical transceiver diameters of 30 to 80 cm. For a transmitted wavelength of 1.55 μm, this ratio is from 7 to 15. This is shown graphically in Fig. 3(a). On the other hand, the spatial extent of the laser beam reaching Earth is significantly lower than the Earth diameter out to ranges of 20 AU or greater, as represented in Fig. 3(b).

Given the relative sizes of the Earth downlink and the laser beam footprint, in order to avoid gross mispointing, first the geometric center of Earth's disc imaged on the optical transceiver focal plane must be determined with sufficient accuracy. Secondly, the offset from the geometrical center to the ground receiver must be derived with sufficient accuracy, and for this knowledge of Earth time at the spacecraft is required. Spacecraft clock accuracies generally are dependent on mission class but typically can be grouped into the 1- to 10-s class or the 1- to 100-ms class. With proper synchronization, it is predicted that Earth time at the spacecraft can be known with an accuracy better than 1 s. With this kind of accuracy in Earth-time knowledge at ranges greater than 0.5 AU, the error contribution to pointing is negligibly small. Both of these topics will be elaborated on in Section IV.

A notion of the required pointing accuracy is indicated by the allocated pointing loss in a typical end-to-end system link budget. Typical pointing budgets allocate about $0.1 * \lambda_{\text{laser}}/D$ each to the radial root-mean-square (rms) jitter and beam mispointing [7]. Approximately 100 to 200 nrad, i.e., $0.03 * (\lambda_{\text{laser}}/D) - 0.06 * (\lambda_{\text{laser}}/D)$, of this usually is allocated to the focal-plane array (FPA) processing errors. So, the problem becomes one of determining whether the Earth centroid determination and errors associated with knowledge of Earth time will allow one to meet this allocation.

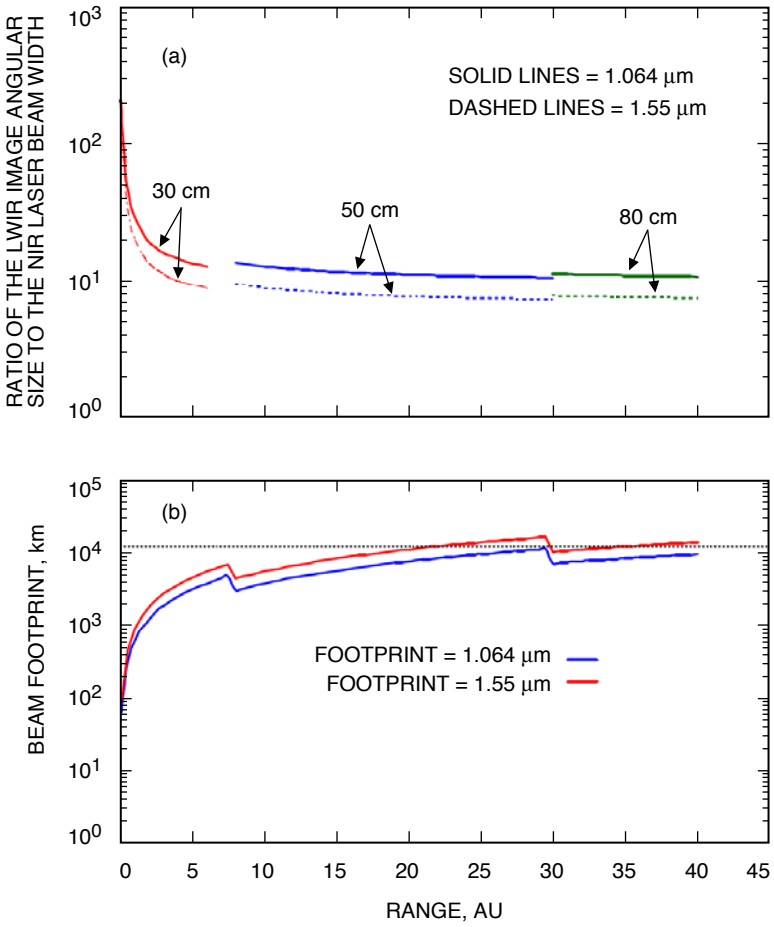

Fig. 3. An optical system that is diffraction-limited at VIS/NIR and LWIR wavelengths: (a) the ratio of the angular sizes of the LWIR-sensed image and the transmitted NIR beam width and (b) the estimated laser beam footprint at Earth as a function of range for the optical transceiver diameters indicated in (a). The dotted horizontal line represents the Earth diameter.

III. Radiometry

Centroiding accuracy will be governed by signal and background photons detected by the LWIR focal-plane sensor and its noise characteristics. In this section, we present analysis to predict the Earth emission signal and accompanying background for the reference design described in Section II.

Assuming the optical transceiver diameter focal ratio to be such that an extended Earth image can form on the focal-plane array, the irradiance, E_{image}, of the image will be given by

$$E_{\text{image}} = T_{\text{sys}} L_e \pi (na)^2 \tag{1}$$

where T_{sys} represents the optical transceiver system loss, L_e is the in-band integrated brightness of the Earth image, and na is the numerical aperture of the optical system. The following relations also apply:

$$na = \sin\theta \approx \frac{1}{f\#} \tag{2a}$$

$$\Omega = \pi \sin^2\theta \tag{2b}$$

$$L_e = \frac{0.01}{\pi} \int_{\lambda_{\min}}^{\lambda_{\max}} \frac{c1}{\lambda^5} \frac{1}{\exp\left(\frac{c2}{\lambda T_e}\right) - 1} \tag{2c}$$

where θ is the half-angle of the cone of light that forms the image, $f\#$ is the focal ratio of the optical transceiver, Ω is the solid angle in steradians, $\lambda_{\min}$ and $\lambda_{\max}$ represent the lower and upper limits of the spectral band used for imaging, T_e is the mean temperature of the Earth, and $c1, c2$ are radiometric constants. Note that if the optical system can resolve Earth then the image irradiance is independent of distance to the Earth and there is no explicit dependence upon the entrance pupil diameter.

At farther distances, when the optical system can no longer resolve Earth and it effectively behaves like a point source, the diffraction-limited system produces an Airy disk. Neglecting effects of the central obscuration, the power within the Airy disk is

$$P_{\text{Airy}} = \frac{\pi}{4} D^2 T_{\text{sys}} E_{\text{ent}} \tag{3}$$

where E_{ent} is the irradiance at the entrance pupil of diameter D. Furthermore, using

$$E_{\text{ent}} = L_e \Omega_e = L_e \pi \left(\frac{r_e}{d_e}\right)^2 \tag{4}$$

where Ω_e is the solid angle subtended by Earth, r_e is the Earth radius, and d_e is the distance to Earth, the Earth image irradiance can be written as

$$E_{\text{image}} = T_{\text{sys}} L_e \pi \left(\frac{r_e}{d_e}\right)^2 \frac{\pi}{4} D^2 \frac{\pi (na)^2}{\lambda^2} \tag{5}$$

In between the two extremes of the extended source and the point source, the image irradiance is the convolution of the geometric image, and the Airy disk indicated by a double asterisk and can be represented by

$$E(r) = \frac{P_{\text{Airy}}}{a^2 b^2} \text{cyl}\left(\frac{r}{a}\right) ** \text{somb}^2\left(\frac{r}{b}\right) \tag{6}$$

where r is the distance from the center of the image, P is the total power in the image, a is the diameter of the geometric Earth image, and b is the half-width of the Airy disk:

$$a = \frac{r_e}{d_e} \frac{D}{(na)} \tag{7}$$

and

$$b = \frac{\lambda}{2(na)} \tag{8}$$

The function cyl(r) is 1 for r less than 1/2 and 0 for r greater than 1/2. The function somb(r) is the Airy disk and is normalized to 1 at the origin.

A. Scatter Properties of Optical Surfaces

Scatter from mirrors, lenses, and windows is caused by surface roughness, refractive index variations, and particulate (dust) contamination. It is commonly observed that the bi-directional reflectance distribution function (BRDF) of clean mirrors and the bi-directional transmittance distribution function (BTDF) of clean lenses has the following functional form, called the Harvey model [8]:

$$\text{BRDF (or BTDF)} = b\left(100\left|\sin\theta - \sin\theta_o\right|\right)^s \tag{9a}$$

where θ is the scatter angle (with respect to the surface normal), θ_o is the specular angle (the direction of reflected or transmitted light from a mirror or lens), and b and s are parameters that vary from one surface to another. The parameter b, called the intercept, is numerically equal to the BRDF in a scatter direction that is 0.01 rad (0.57 deg) from the specular direction. The parameter s is the slope of the BRDF function when it is plotted on a log-log scale (the logarithm of the BRDF as a function of the logarithm of $\sin\theta - \sin\theta_o$). For most mirrors and lenses, the parameters b and s fall within the ranges

$$0.01 < b < 1 \tag{9b}$$

and

$$-3 < s < -1 \tag{9c}$$

These parameters are not functions of the lens or mirror material, but rather are functions of the surface roughness characteristics and refractive index variations within the material of transmissive optics.

Scatter from particulate contamination was studied by Spyak and Wolfe [9]. They found that the BRDF from contamination was well-fit (to within a factor of 2 or 3) by the Mie theory of scatter. Mie calculations, combined with particulate size distributions of the form given by the Institute of Environmental Sciences and Technology (IEST) contamination standard [10], result in BRDFs of the form

$$\rho_c = b_1\left(1 + \frac{\left(\sin\theta - \sin\theta_o\right)^2}{l_1^2}\right)^{s_1/2} + b_2\left(1 + \frac{\left(\sin\theta - \sin\theta_o\right)^2}{l_2^2}\right)^{s_2/2} \tag{10}$$

Fits to the Mie calculations performed by Dittman [11] result in the tables of coefficients given in Tables 1 and 2 for wavelengths of 1.15 μm and 10 μm, respectively. The coefficients b_1 and b_2 are proportional to the particulate coverage fraction for each contamination level.

Table 1. Contamination level, coverage fraction, and BSDF coefficients for a wavelength of 1.15 μm.

Contamination level	Coverage fraction, ppm	b_1	s_1	l_1	b_2	s_2	l_2
100	2.5	0.32	−2.7	0.001	5×10^{-7}	−0.5	0.1
200	42	5.4	−2.7	0.001	8×10^{-6}	−0.5	0.1
300	253	33	−2.7	0.001	5×10^{-5}	−0.5	0.1
400	982	130	−2.7	0.001	2×10^{-4}	−0.5	0.1
500	2900	370	−2.7	0.001	6×10^{-4}	−0.5	0.1

Table 2. Contamination level, coverage fraction, and BSDF coefficients for a wavelength of 10.0 μm.

Contamination level	Coverage fraction, ppm	b_1	s_1	l_1	b_2	s_2	l_2
100	2.5	0.004	−2.6	0.0085	1×10^{-7}	0	NA
200	42	0.069	−2.6	0.0085	2×10^{-6}	0	NA
300	253	0.417	−2.6	0.0085	1×10^{-5}	0	NA
400	982	1.618	−2.6	0.0085	4×10^{-5}	0	NA
500	2900	4.78	−2.6	0.0085	1×10^{-4}	0	NA

B. Point Source Transmission

Point source transmission (PST) is a measure of an optical system's stray-light transmission. It is sometimes called normalized detector irradiance (NDI) or point source normalized detector irradiance (PSNDI). For a distant point source that is outside an optical system's field of view, PST is defined as the stray-light irradiance at the detector, E_{det}, divided by the irradiance from the source, E_{source}, at the entrance to the system:

$$\text{PST} = \frac{E_{\text{det}}}{E_{\text{source}}} \tag{11}$$

The irradiance of the source is measured on a plane that is perpendicular to a line from the system to the source, as illustrated in Fig. 4. The detector stray-light irradiance varies with source direction, so PST is a function of the source direction. The stray-light irradiance also varies with position on the detector, so the PST does too.

Given the PST, the detector irradiance from a given source is obtained from Eq. (9) multiplying by the source irradiance at the entrance to the system:

$$E_{\text{det}} = E_{\text{source}}\text{PST} \tag{12}$$

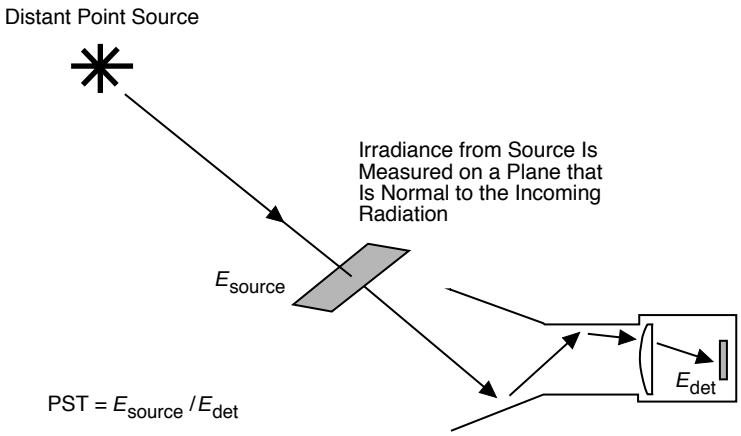

Fig. 4. Illustration of point-source geometry for the definition of PST.

C. Stray Light from the Window

The window sits in front of the telescope, where it is illuminated fully by the Sun (the baffle does not shade the window). The brightness of the light that is scattered by the window is given by the window's BTDF:

$$L_w = \rho_w E_s \cos\theta \tag{13}$$

where ρ_w is the BTDF, E_s is the in-band solar irradiance, and θ is the angle between the Sun and the line of sight (LOS) of the telescope. If the angle subtended by the Sun is small, then

$$E_s = L_s \pi \sin^2 \alpha \tag{14}$$

where L_s is the in-band radiance of the Sun and α is the half-angle subtended by the Sun.

To relate the brightness of the window to the detector irradiance and PST, recall that brightness is a conserved quantity in an optical system, except for transmission losses. If the transmission of the telescope is T, then the detector irradiance produced by the window with brightness L_w is

$$E_{\mathrm{det}} = L_w T \pi (na)^2 \tag{15}$$

where na is the system numerical aperture. Substituting Eq. (10) for L_w and dividing by E_s gives

$$\frac{E_{\mathrm{det}}}{E_s} = \mathrm{PST} = T \rho_w \pi (na)^2 \cos\theta \tag{16}$$

D. Stray Light from the Baffle and Primary Mirror

The primary mirror is shaded by the baffle when the Sun is far enough off-axis. Light then must scatter from the inside baffle as well as the mirror before it can propagate to the detector. This complicates the analysis greatly, but approximate formulas for estimating the PST from the baffle and mirror are given by Greynolds [12]. These formulas include scatter from the mirror alone (when the Sun angle is low enough to illuminate the primary mirror directly), scatter from baffle cavities, scatter from vane edges within the baffle, and diffraction from the vane edges.

Both the expressions and their derivations are lengthy, so they will not be transcribed here. Interested readers are referred to [12].

E. Extended Source Integration

At distances below 1 AU, the Sun is not well-approximated as a point source. For example, at 0.1 AU the Sun subtends a full angle of 5.3 deg. To calculate the stray-light irradiance, it is necessary to integrate over the solar disk.

Figure 5 illustrates the geometry of the telescope and Sun. The angle between the telescope line of sight and the edge of the Sun is θ, and the Sun subtends a half-angle, α. An arbitrary location on the solar disk is specified by polar coordinates θ_s and φ_s, with the polar axis along a line from the telescope to the center of the Sun, and $\varphi_s = 0$ along the arc from the center of the Sun to the telescope line of sight. We may define three unit vectors that are shown in Fig. 6. The vector $\mathbf{u_s}$ points toward the center of the

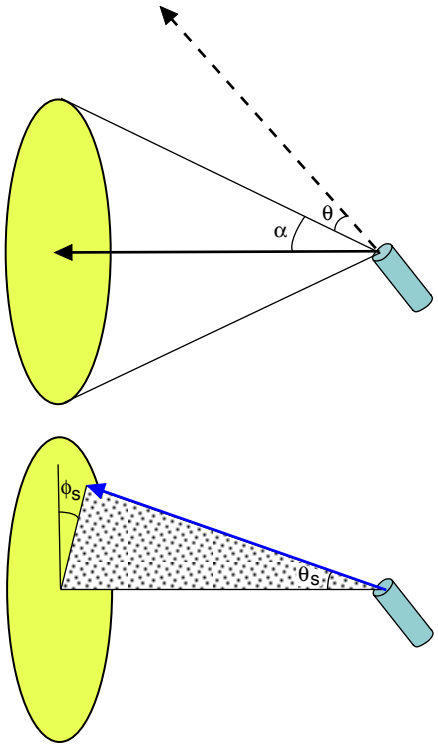

Fig. 5. Illustrations of geometry and angles for extended source integration.

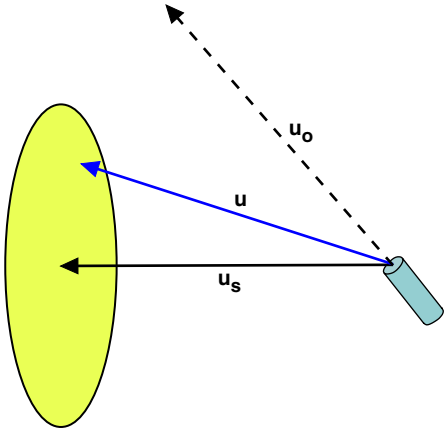

Fig. 6. Illustration of unit vectors for extended source integration.

Sun. The vector $\mathbf{u_o}$ points along the telescope line of sight. The vector $\mathbf{u}$ points to an arbitrary location on the Sun. If we define a right-handed Cartesian coordinate system with $\mathbf{z}$ parallel to $\mathbf{u_s}$, and $\mathbf{y}$ in the plane defined by $\mathbf{u_s}$ and $\mathbf{u_o}$, then we may express the three unit vectors in terms of θ, α, θ_s, and φ_s:

$$\mathbf{u_s} = \mathbf{z} \tag{17}$$

and

$$\mathbf{u_o} = \sin(\theta + \alpha)\mathbf{y} + \cos(\theta + \alpha)\mathbf{z} \tag{18}$$

and

$$\mathbf{u} = -\sin\theta_s \sin\varphi_s \mathbf{x} + \sin\theta_s \cos\varphi_s \mathbf{y} + \cos\theta_s \mathbf{z} \tag{19}$$

Now, for axially symmetric telescopes, the stray light from a point on the Sun depends upon only the angle between the telescope line of sight and the line to the point. Call this angle γ. We obtain an expression for γ by taking the dot product of $\mathbf{u}$ and $\mathbf{u_o}$:

$$\cos\gamma = \mathbf{u} \cdot \mathbf{u_o} = \sin(\theta + \alpha)\sin\theta_s \cos\varphi_s + \cos(\theta + \alpha)\cos\theta_s \tag{20}$$

We may now express the stray light from the Sun in terms of an integral over the solar disk. Let $P(\gamma)$ be the point source transmission (PST) of the telescope. Then the stray-light irradiance at the detector is

$$E(\theta) = L_s \int_0^{2\pi} \int_0^{\alpha} P(\gamma) \sin\theta_s d\theta_s d\varphi_s \tag{21}$$

where L_s is the in-band solar radiance (brightness, W/mm^2-sr) of the Sun.

F. Diffraction from Spiders

When the spiders that hold a secondary mirror are illuminated by the Sun directly, some of this sunlight is diffracted, or bent, into the shadow region and enters the field of view. Figure 7 illustrates this. The irradiance of this diffracted light may be estimated with expressions for diffraction from a straight edge, or with the boundary wave diffraction theory. Both of these are discussed by Born and Wolfe [13]. For this article, we start with an expression for the irradiance in the shadow of a straight edge that is illuminated by a plane wave. We then use this expression and the Lagrange invariant of an optical system to derive the irradiance from diffracted light at the focal plane of a telescope.

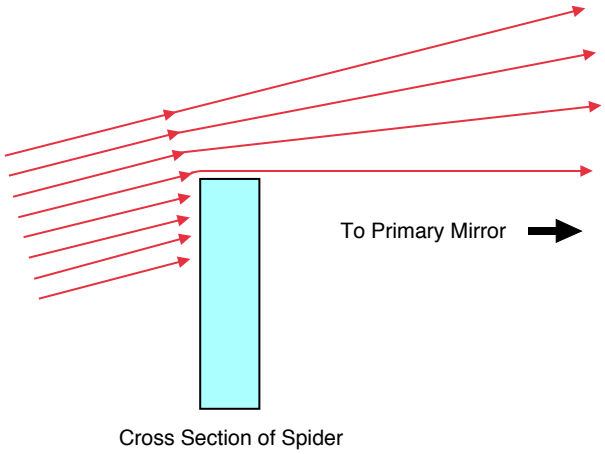

Fig. 7. Illustration of diffraction of light around a spider obscuration.

For a plane wave incident on a straight edge, the irradiance on a small collecting area (located in the shadow of the edge) a distance L from the edge, as illustrated in Fig. 8, is given by

$$E = E_o \frac{1}{4\pi^2} \frac{\lambda}{L} \frac{1}{\sin^2 \theta} \tag{22}$$

where λ is the wavelength of the plane wave. Define a coordinate system in which x runs along the edge, y is perpendicular to the edge, and z is parallel to the optical axis of the telescope. We consider the contribution from a small portion of the Sun that subtends an angle $\Delta\alpha$ in the x-direction and $\Delta\beta$ in the y-direction. The irradiance E_o is then

$$E_o = L_s \Delta\alpha \Delta\beta \tag{23}$$

where L_s is the brightness of the Sun. Diffraction by the edge spreads this light out along the y-direction, but not along the x-direction. We now transfer this diffracted light to the focal plane of the telescope. Figure 9 shows a portion of the light from the edge that is diffracted into a small angular range $\Delta\theta$ centered about an angle θ. This narrow range of angles is focused within a narrow band of width Δy on the detector. We can relate $\Delta\theta$ to Δy through the Lagrange invariant:

$$D\Delta\theta = 2(na)\Delta y \tag{24}$$

where D is the diameter of the entrance pupil (which is usually the primary mirror) and na is the numerical aperture at the focal plane. Similarly, the light from the portion of the Sun that subtends an angle $\Delta\alpha$ in the x-direction is focused onto the detector over a width Δx, where

$$D\Delta\alpha = 2(na)\Delta x \tag{25}$$

To calculate the irradiance on the detector, we first calculate the power falling on the mirror within the angle $\Delta\theta$. From Eqs. (22) and (23) and Fig. 9, this power is the irradiance at the mirror times the area of a band of width D and height Δy:

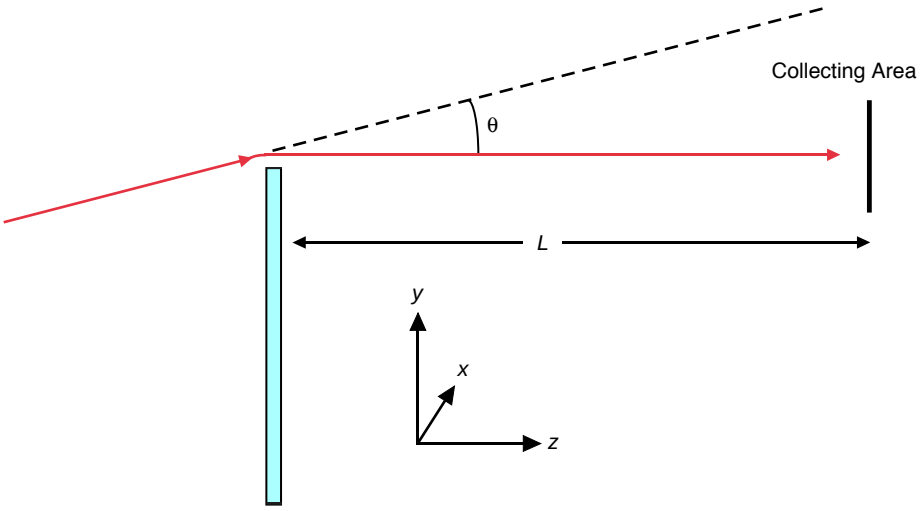

Fig. 8. Illustration of diffraction geometry.

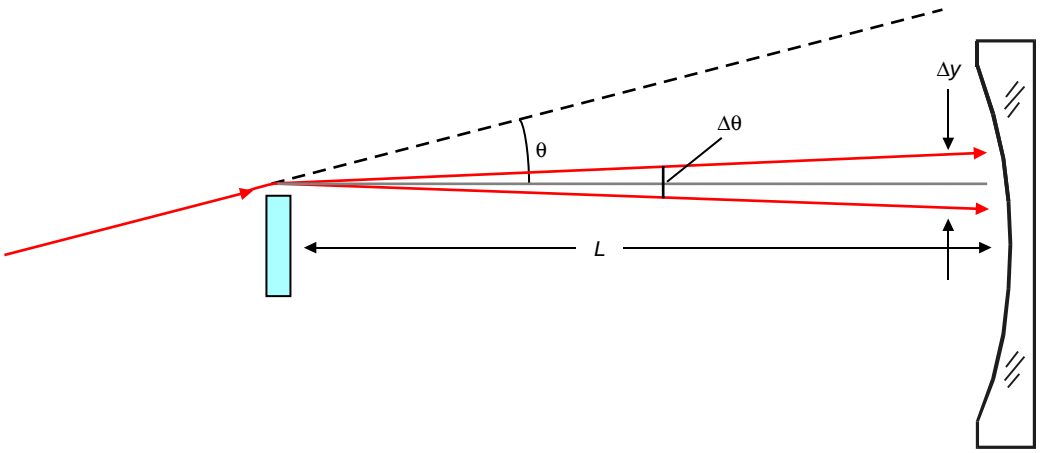

Fig. 9. Illustration of angles and interval over which a portion of the diffracted light is collected by the primary mirror.

$$dP = E\,D\,\Delta y = L_s \Delta\alpha \Delta\beta \frac{1}{4\pi^2}\,\frac{\lambda}{L}\,\frac{1}{\sin^2\theta} D \Delta y \tag{26}$$

But $\Delta y/L$ is $\Delta\theta$, so we may rewrite Eq. (26) as

$$dP = L_s \Delta\beta \frac{1}{4\pi^2}\,\frac{\lambda}{D}\,\frac{1}{\sin^2\theta} D^2 \Delta\theta \Delta\alpha \tag{27}$$

where we have also multiplied and divided by D and brought $\Delta\alpha$ to the end of the equation. Now the power falling within the indicated band on the mirror is transferred to an area $\Delta x \Delta y$ on the detector, except for transmission losses. Multiplying Eq. (27) by the transmission, T, and using Eqs. (24) and (25), we get the following expression for the power falling in the area $\Delta x \Delta y$:

$$dP = L_s T \Delta\beta \frac{1}{4\pi^2} \frac{\lambda}{D} \frac{1}{\sin^2\theta} 4(na)^2 \Delta y \Delta x \tag{28}$$

Divide both sides by $\Delta y \Delta x$ to obtain the detector irradiance from a portion of the Sun that subtends a solid angle $\Delta\alpha\Delta\beta$:

$$dE = \frac{dP}{\Delta x \Delta y} = L_s T \frac{1}{\pi^2} \frac{\lambda}{D} (na)^2 \frac{1}{\sin^2\theta} \Delta\beta \tag{29}$$

To obtain the detector irradiance from the full Sun, we must integrate the vertical dimension of the Sun's disk. In Eq. (26), the small angle $\Delta\beta$ assumes the role of a differential angle $d\theta$. We then integrate over θ to get

$$E = L_s T \frac{1}{\pi^2} \frac{\lambda}{D} (na)^2 \int_{\theta_{\min}}^{\theta_{\max}} \frac{1}{\sin^2\theta} d\theta \tag{30}$$

Usually, both edges (bottom and top, or left and right) of a spider are illuminated by the Sun, so we get a contribution from both edges. To account for this, we multiply Eq. (30) by 2, and denote the final result by E_{dif}:

$$E_{\text{dif}} = L_s T \frac{2}{\pi^2} \frac{\lambda}{D} (na)^2 \int_{\theta_{\min}}^{\theta_{\max}} \frac{1}{\sin^2\theta} d\theta \tag{31}$$

If the angle subtended by the Sun is small compared to the diffraction angle θ, then we may replace the integral with the product of the integrand and the subtended angle of the Sun, $\Delta\theta_s$:

$$E_{\text{dif}} \approx L_s T \frac{2}{\pi^2} \frac{\lambda}{D} (na)^2 \frac{1}{\sin^2\theta} \Delta\theta_s \tag{32}$$

G. Stray Light from the Transmitter

Many of the optical components in the system are shared by the acquisition and tracking system and the laser transmitter. Some of the laser light that is incident on these components is scattered back to the acquisition and tracking detector. If the power from the laser is P, then the irradiance incident on an optical component is approximately

$$E = T_1 \frac{P}{\pi r^2} \tag{33}$$

where r is the radius of the beam on the component and T_1 is the transmission from the laser to the optical component. The brightness of the scattered light is

$$L = \rho E \tag{34}$$

where ρ is the BSDF. Using conservation of brightness, except for a transmission of T_2 from the component to the detector, the detector irradiance is

$$E = T_2 L \pi (na)^2 = T_2 T_1 \rho \frac{P}{\pi r^2} \tag{35}$$

H. Internal Thermal Irradiance

Warm surfaces within the system that are visible to the detector emit thermal radiation that is collected by the detector. The internal thermal irradiance may be calculated using the equation for a blackbody. The in-band brightness, or radiance, of a blackbody with temperature T is

$$L_i = \frac{1}{\pi} \int_{\lambda_{\min}}^{\lambda_{\max}} \frac{c_1}{\lambda^5} \frac{1}{\exp\left(\frac{c_2}{\lambda T}\right) - 1} d\lambda \tag{36}$$

where c_1 and c_2 are constants:

$$c_1 = 3.7415 \times 10^4 \quad \text{W-}\mu\text{m}^4/\text{cm}^2 \tag{37}$$

and

$$c_2 = 1.43879 \times 10^4 \quad \mu\text{m-K}^4 \tag{38}$$

Using the above constants, the units of L_i are W/cm^2-sr. Multiply Eq. (36) by 0.01 to convert to W/mm^2-sr. Given L_{bb}, the detector irradiance from a surface with emissivity ε is

$$E = T_{opt} \varepsilon L_{bb} \Omega \tag{39}$$

where Ω is the solid angle subtended by the surface (as seen from the detector) and T_{opt} is the net transmission of the optical components between the detector and the radiating surface.

The thermal irradiance from optical surfaces is readily calculated using the above formulas. Because all of these surfaces fill the exit pupil of the system, they all subtend the same solid angle,

$$\Omega = \pi (na)^2 \tag{40}$$

so the irradiance is given by

$$E = T_{opt} \varepsilon L_{bb} \pi (na)^2 \tag{41}$$

The total irradiance is the sum of all of the contributors.

The contributions discussed were all plotted as the optical power on a focal-plane-array pixel versus Sun angle in Fig. 10. From Fig. 10, it is apparent that by far the dominant contribution to background light on the LWIR focal plane is the internal thermal emission from the optical components of the transceiver. This is significant because most flight optics are tested at room temperature and maintained close to room temperature during space operations. The example depicted in Fig. 10 suggests that maintaining the optics at a cooler temperature would benefit the signal-to-noise ratio (SNR) that governs the centroiding accuracy. This may entail pre-flight testing of cooled optics, with the associated cost and

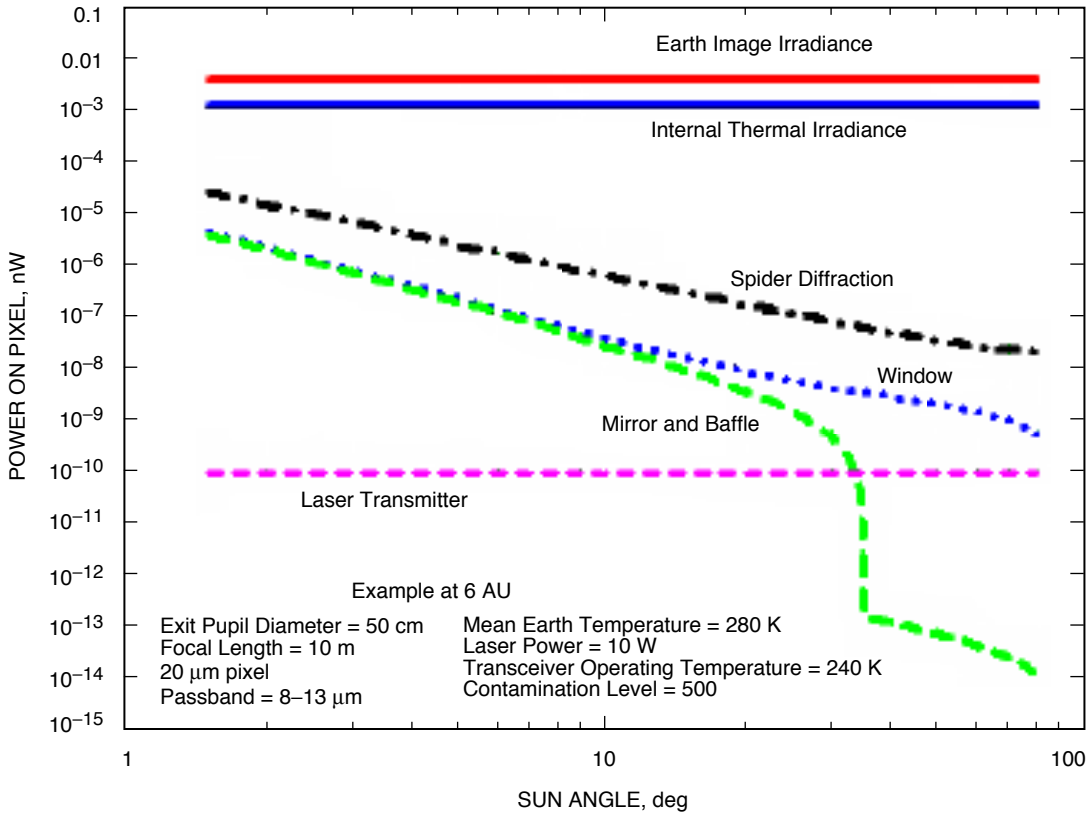

Fig. 10. An example of a radiometric estimation of an Earth signal and all components of the background contribution incident on the LWIR focal-plane array.

complexity. Figures 11(a) through 11(f) present examples for a number of optical transceiver aperture diameters, instantaneous fields of view (IFOVs), and transmitter beam widths, where the average Earth signal per pixel is plotted as a function of range. Horizontal lines showing the internal thermal irradiance corresponding to soak temperatures of the optics are also shown. Thus, the extent of cooling required as a function of mission range and other associated parameters can be inferred. At ranges from which Earth image tracking would be preferred, internal optics soak temperatures cooler than 295 K are suggested, and the temperature decreases with longer ranges. Note that this preliminary analysis does not take into account situations where internal thermal gradients may arise due to nonuniform solar illumination.

IV. Estimated Earth Emission Nonuniformity and Its Effects on Centroiding

Previous theoretical studies [14,15] have shown that the Cramer–Rao lower bound (CRLB) on the rms error in estimating image position on an array detector can be made arbitrarily small when the spatial light distribution of the pointing reference is precisely known. This can be achieved, in theory, by increasing the integration time to build up the SNR. On the other hand, when the spatial intensity distribution is not known in sufficient detail, the lower bound does not decrease linearly with SNR but reaches a floor beyond which increasing integration time will not reduce the error. The LWIR Earth image falls in the latter category, where nonuniform emissivity causes the sensed Earth image to have a light distribution that is not mathematically well described. Moreover, varying and unpredictable cloud cover combined with Earth's rotation further perturb the unknown spatial light distribution. Further analysis dealing with the CRLB is presented in [16].

In this article, an empirical approach is adopted for addressing this problem. We used infrared measurements of Earth from space, obtained with the Atmospheric Infrared Sounder (AIRS) instrument

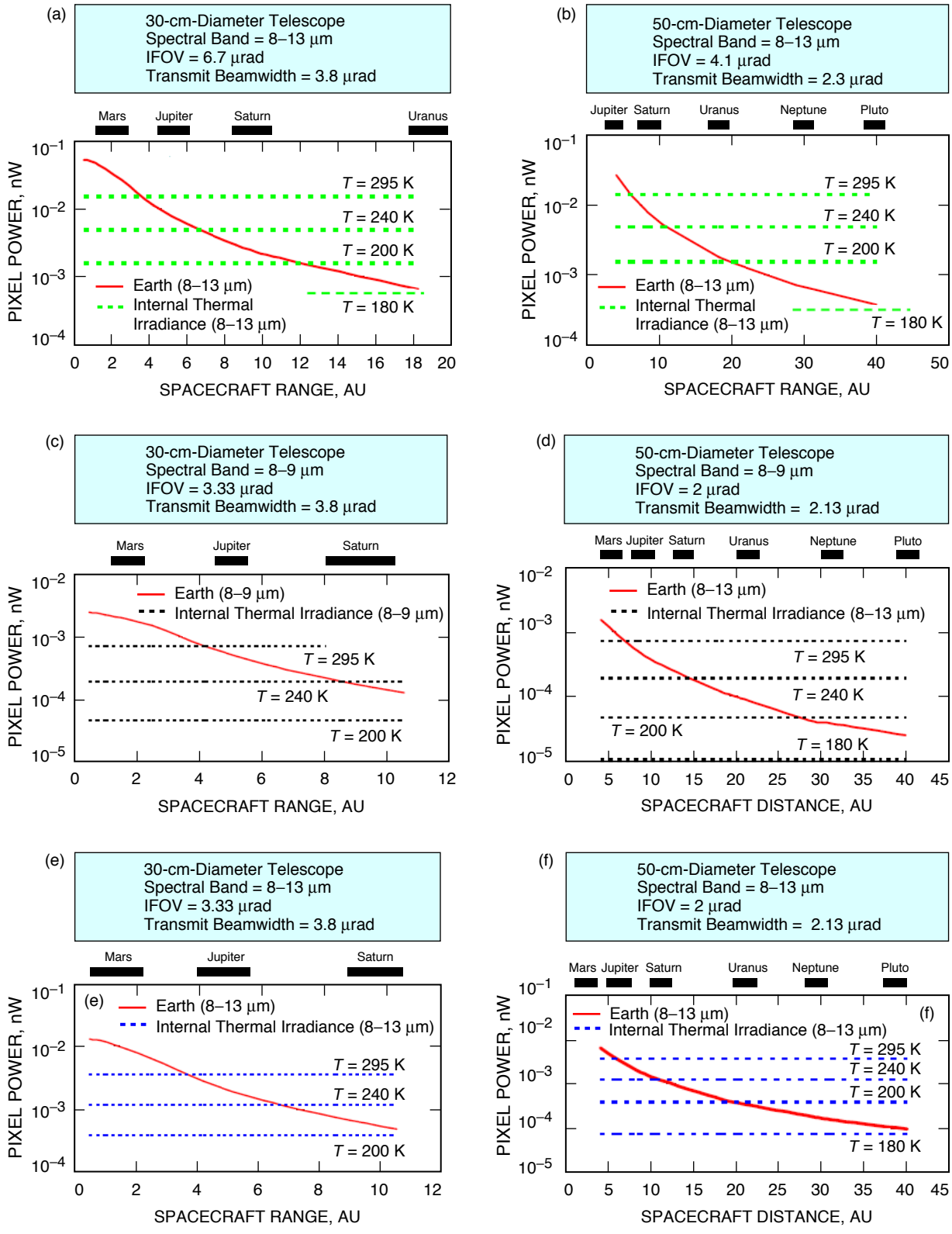

Fig. 11. Examples for a number of optical transceiver aperture diameters, instantaneous fields of view (IFOVs), and transmitter beam widths, where the average Earth signal per pixel is plotted as a function of range.

onboard the Aqua satellite in Sun-synchronous orbit. The data were acquired using multiple channels that overlapped our spectral region of interest. Swaths of data obtained utilizing multiple spectral channels were entered into a database. Earth images were synthesized by piecing together these data. The details of the Earth image synthesis will be the topic of a future article. For the sake of completeness, a brief description is provided here. AIRS sensors acquire Earth temperatures over 40,000 points uniformly distributed over the globe. The temperature data are converted to emissivity over the spectral bands of the AIRS sensors. Using the geometrical center of the Earth image as seen from deep space, an orthographic projection of Earth is created in order to obtain a disc of Earth that will be "seen" by a focal-array sensor in deep space. The center of the Earth image is projected on the center of an $N \times N$ pixel array, with N being odd. N is usually taken to be 255. This $N \times N$ pixel image of Earth is convolved with the optical transfer function of the imaging system, a second $M \times M$ pixel array, where M is mandated to be odd. The resulting image has $(N + M - 1) \times (N + M - 1)$ pixels. The center of the new image is then $[(N + M - 1)/2, (N + M - 1)/2]$. Because the pixel IFOV at the sensor focal plane is larger than the pixel angular extension of the high-definition image (especially at large range), it is necessary to crop the image, using as the new pixel size the one dictated by the sensor IFOV. The resulting final image will have pixel dimension $L \times L$, with $L < (N + M - 1)$. Given the fact that the center of the initial high-definition image on the focal plane is exactly known, so will be the final one.

Here we show some of the synthesized images and address processing of these images with simple centroiding algorithms. A MATLAB graphical user interface (GUI) was created for accessing the AIRS database. Furthermore, a number of relevant parameters, listed below, can be selected:

- Earth image pixellation (determines the resolution of a temperature grid used to map the thermal image of Earth).
- Spectral band from 8 to 13 μm.
- Spacecraft range from Earth.
- Sun–Earth–probe angle that can be used to generate daytime or nighttime Earth images. Note that the spacecraft is assumed to be in the ecliptic in the present version of the MATLAB GUI, consistent with planetary missions.
- Focal-plane array characteristics, such as
  - Dark noise
  - Pixel size
  - Responsivity corresponding to the spectral band chosen
  - Exposure time
  - Full-well capacity
  - Number of image frames to generate.
- System parameters, such as
  - Optical transceiver diameter
  - Optical transceiver focal length
  - Optical transceiver efficiency at the spectral band
  - IFOV on the camera
  - Background noise incident per pixel.

Note that in the current version the read-noise, dynamic range, and analog-to-digital conversion characteristics are not addressed.

Figure 12(a) shows a simulated temperature map of the Earth based on AIRS measurements. In this view, the African continent is in the center of the image with the colder (green-blue) patches representing clouds. The image corresponds to a spectral band of 8 to 13 μm. Figure 12(b) shows simulated focal-plane images for a 30-cm aperture diameter optical system (including a 20 percent linear obscuration) and an IFOV of 4 μrad. These images were synthesized assuming that the optical system is viewing Earth from different ranges, as annotated in Fig. 12(b). At closer ranges with a larger angular size of the Earth, the effects of emissivity nonuniformity are dominant. Thus, using the AIRS data, we have been able to synthesize representative renditions of the Earth image viewed from different distances. This provides a very powerful simulation tool since LWIR images acquired from spacecraft at varying ranges are not readily available. The image shown in Fig. 1 was a rare instance of such an image. An Earth image was synthesized using the same viewing distance and optical system used for recording the image shown in Fig. 1. The comparison is qualitative due to the fact that the images are related to data acquired on different days. Figure 13 shows this comparison. The qualitative similarities in terms of the location of the cold South Pole and the range of temperatures provide a sanity check on the validity of the image synthesis approach adopted in this article.

The synthesized Earth images were analyzed using center-of-mass and edge-detection centroiding algorithms in order to gain an understanding of position accuracies that could be derived from LWIR Earth images. Background and sensor noise typical for a quantum-well infrared photodetector (QWIP) array camera were added to the synthesized image. The center-of-mass centroiding algorithm was used, with the centroid coordinates on the image plane, x_c and y_c, defined as

$$x_c = \frac{\sum_{i=1}^{N}\sum_{j=1}^{N}(i-0.5)I_{ij}}{\sum_{i=1}^{N}\sum_{j=1}^{N}I_{ij}} \tag{42a}$$

$$y_c = \frac{\sum_{i=1}^{N}\sum_{j=1}^{N}(j-0.5)I_{ij}}{\sum_{i=1}^{N}\sum_{j=1}^{N}I_{ij}} \tag{42b}$$

Here the subscripts i, j represent the pixel numbers in orthogonal directions, whereas I represents the sensed signal on the (i, j)th pixel in an image plane covered by $N \times N$ pixels; x_c and y_c represent the geometrical center-of-mass or centroid of the incident signal. In all our analysis from this point on we assumed sensors that were limited by background noise. In other words, the noise contribution of background light was much stronger than dark and read-noise combined. This is an appropriate assumption for QWIP sensors.

In Eq. (42), offset contributions arising due to additive background on the pixels is mitigated by windowing around the area containing the signal and subtracting the background. The method for choosing the optimal window for centroid processing and estimating background levels is as follows. The Earth image is uniformly pre-filtered in order to average out the background noise. A histogram of the filtered image is then used to determine the average background noise value by identifying its first (and strongest) peak in the signal histogram of the pixels. This average is subtracted from the filtered image with the additional caveat that all pixels with negative values be set to zero. The center-of-mass equation described by Eq. (42) is then used, and the centroid values are determined. Figure 14 shows the algorithm used as a flow diagram, Fig. 14(a), and graphically, Fig. 14(b).

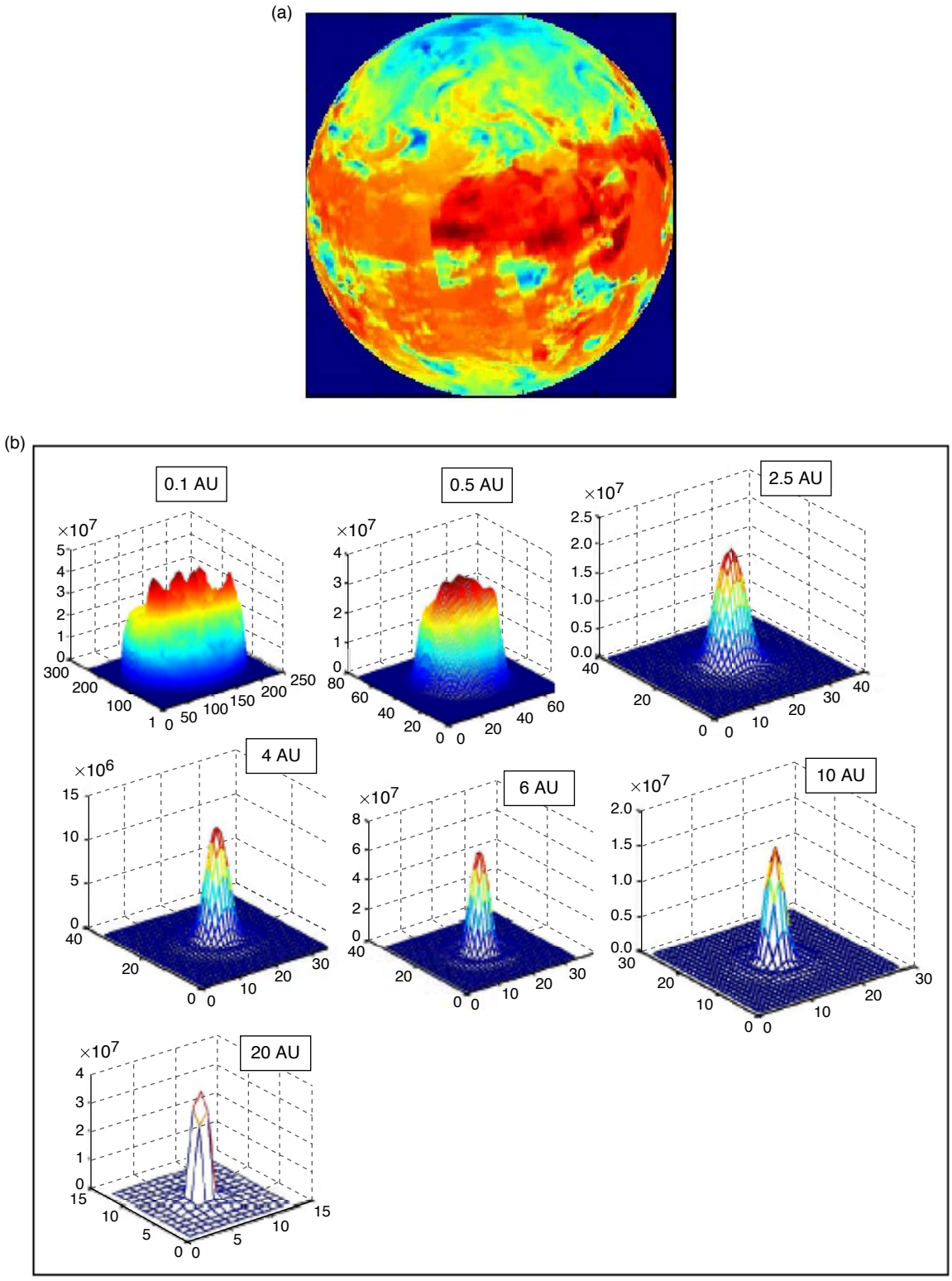

Fig. 12. Results of synthesized Earth thermal images viewed from deep space, using data gathered by near-Earth-orbiting spacecraft: (a) synthesized temperature map of Earth showing clouds (colder shades of blue and green) over Africa and (b) focal-plane images synthesized as a function of range.

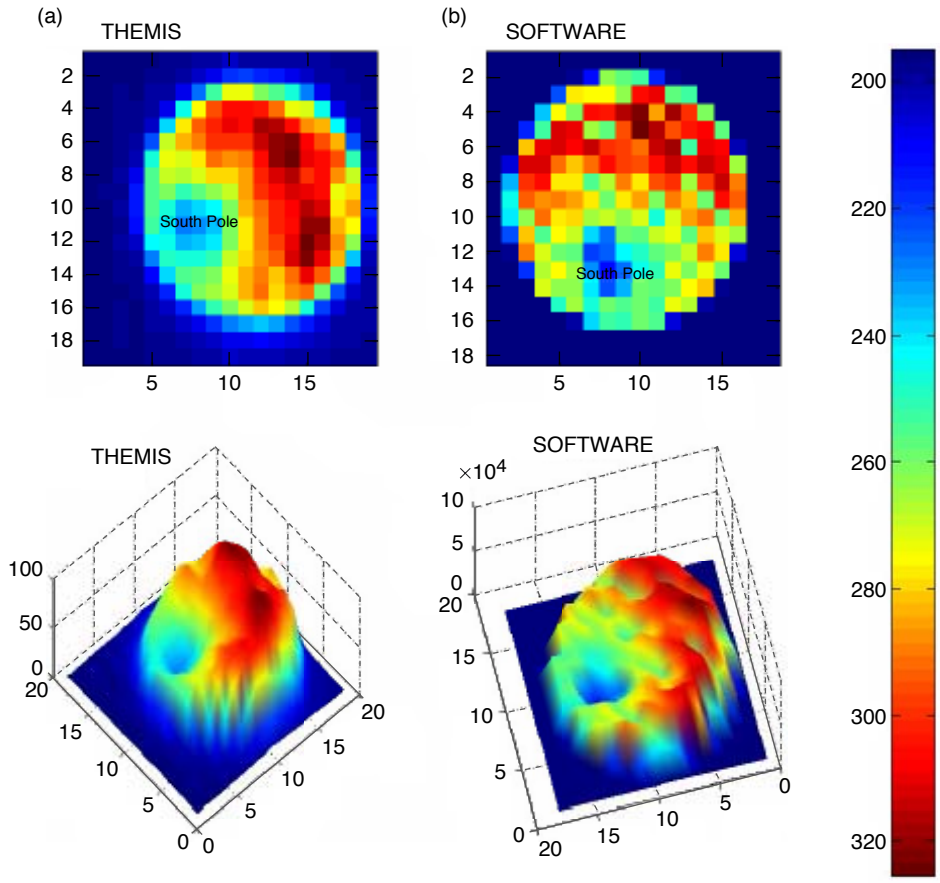

Fig. 13. A comparison between (a) a measured thermal image of Earth obtained using the THEMIS instrument onboard the Mars Odyssey spacecraft taken from 0.2 AU and (b) a simulated image using AIRS data. The differences arise from nonidentical Earth temperature distributions from when the measurements were made and when the AIRS data were gathered. The similarity in terms of the location of the cold South Pole and of the range of temperatures represented by the measurement and simulation is noteworthy.

The centroiding procedure described above can be further improved by utilizing known information about the link, such as spacecraft range from Earth, aperture size, center wavelength, and IFOV. This is represented by the alternate flow diagram shown in Fig. 15.

Figure 16 shows representative results obtained using the centroiding algorithm just described. In Fig. 16(a), a QWIP sensor with a narrowband spectral responsivity spanning 8 to 9 μm, and typical noise characteristics, was assumed. Moreover, in Fig. 16(a) an aperture diameter of 30 cm, an IFOV of 4 μrad, an internal optics temperature of 290 K, and ranges out to 6 AU are represented. In Fig. 16(b), a broadband QWIP with spectral response from 8 to 13 μm was assumed. The aperture diameter and IFOV in Fig. 16(b) were 30 cm and 3.3 μrad for 2.5 to 6 AU and 50 cm and 2 μrad for ranges from 10 to 20 AU. Finally, in Fig. 16(b) the internal optics temperature was 240 K for the closer ranges and 200 K for the farther ranges. The integration times used were consistent with avoiding pixel saturation by accumulated Earth signal and background. The images synthesized for centroid determination assume ideal optics, and the contributions of the effects of pixel nonuniformity to centroiding errors were neglected in the analysis represented by Fig. 16.

For each condition analyzed in Fig. 16, a sequence of 1000 image frames was simulated, including sensor and background noise effects. The centroid for each image frame was calculated, and from these

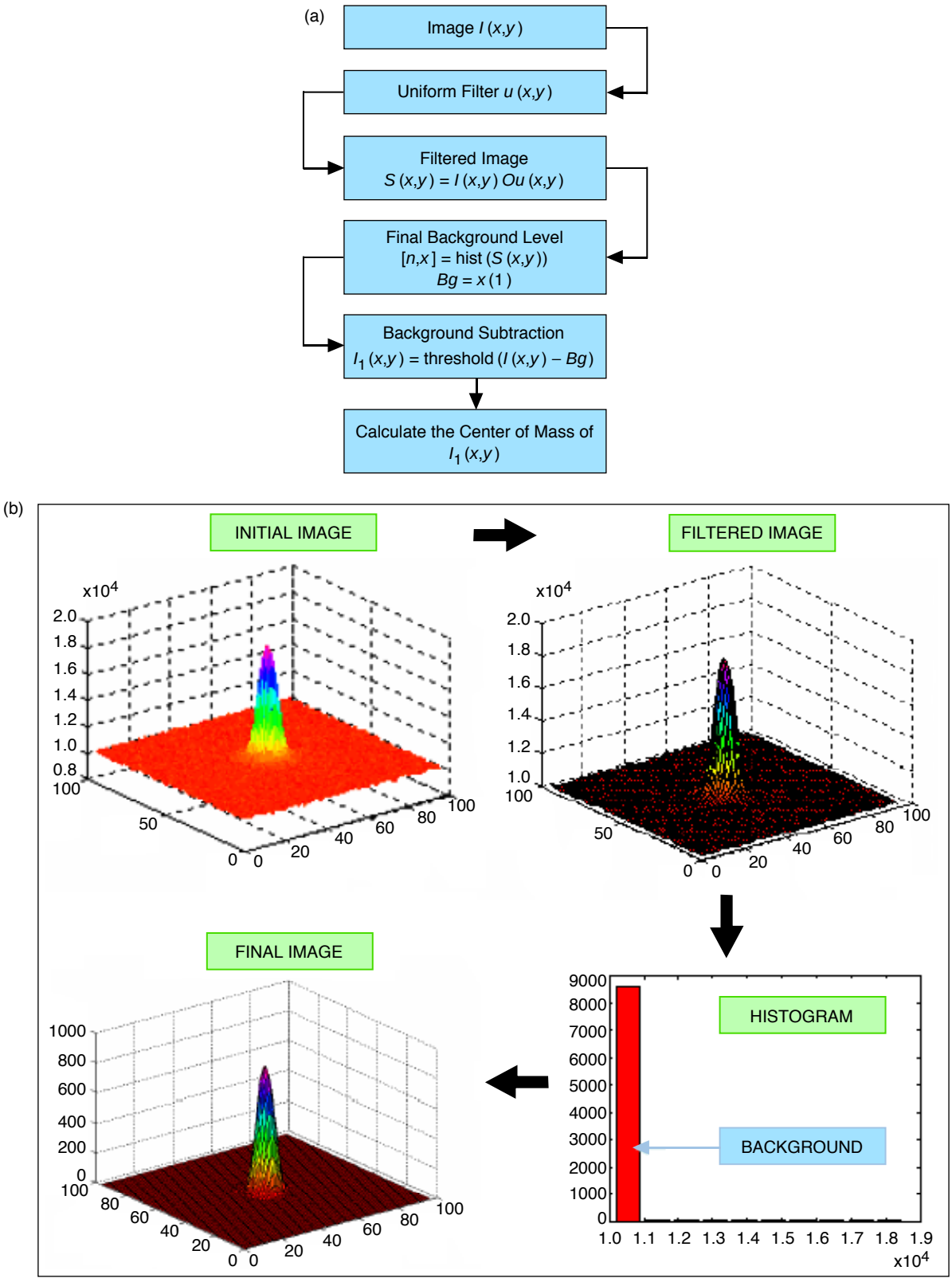

Fig. 14. The sequence used for processing images for centroiding shown (a) as a flow diagram and (b) graphically.

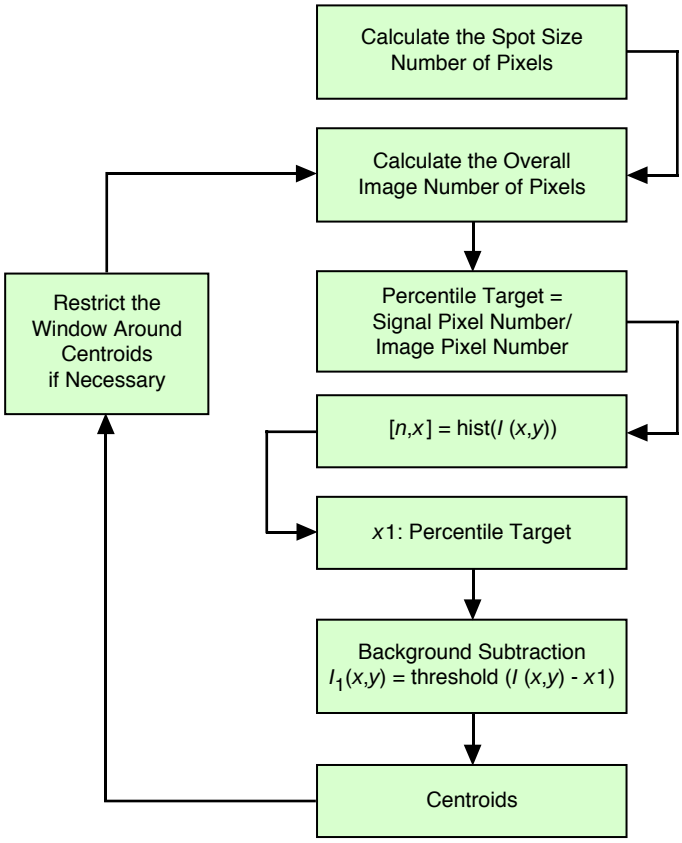

Fig. 15. A centroid processing flow diagram, where the link information, such as distance, aperture diameter, and center of spectral band, is utilized to refine centroid determination.

values a mean geometrical center and variance were determined. The offset of the mean geometrical center from a pre-defined pixel coordinate set during image synthesis is shown as the bias error. Note that the bias determination is possible because the image center is well-known due to the manner in which the image was synthesized, as described above. The standard deviation was equivalent to the jitter contribution of the error. Finally, the total error is given by bias + 3*jitter. Note that jitter here refers to noise equivalent angle (NEA) contributions only and not to uncompensated mechanical vibrations.

Although the signal is reduced because of the limited responsivity of the narrowband QWIP, the noise characteristics of the sensor and the background are also reduced, whereas the broadband QWIP that provides a stronger signal also has higher dark noise and gathers a larger fraction of background noise.

The underlying conclusion from Figs. 16(a) and 16(b) is that the jitter error stays below 100 nrad for either choice of sensor and out to the very long ranges treated in the analysis. However, an offset or bias error that is of the order of 1 μrad at the ranges of interest always seems to be present. Given the allocations from a pointing budget, this bias error very likely would violate the allocation, as pointed out in Section III. We believe the bias errors are caused by the spatial nonuniformity that owes its origin to the emissivity variations. In Fig. 16, we showed the center-of-mass algorithm results, and we also analyzed image processing using an edge-detection technique and found similar results. Therefore, the need for finding more sophisticated image processing in order to reduce bias error was identified. The preliminary analysis emphasizes the need for a suitable algorithm that would mitigate this offset. The mitigation approach was not formulated at the time this article was written and will be worked on in the future.

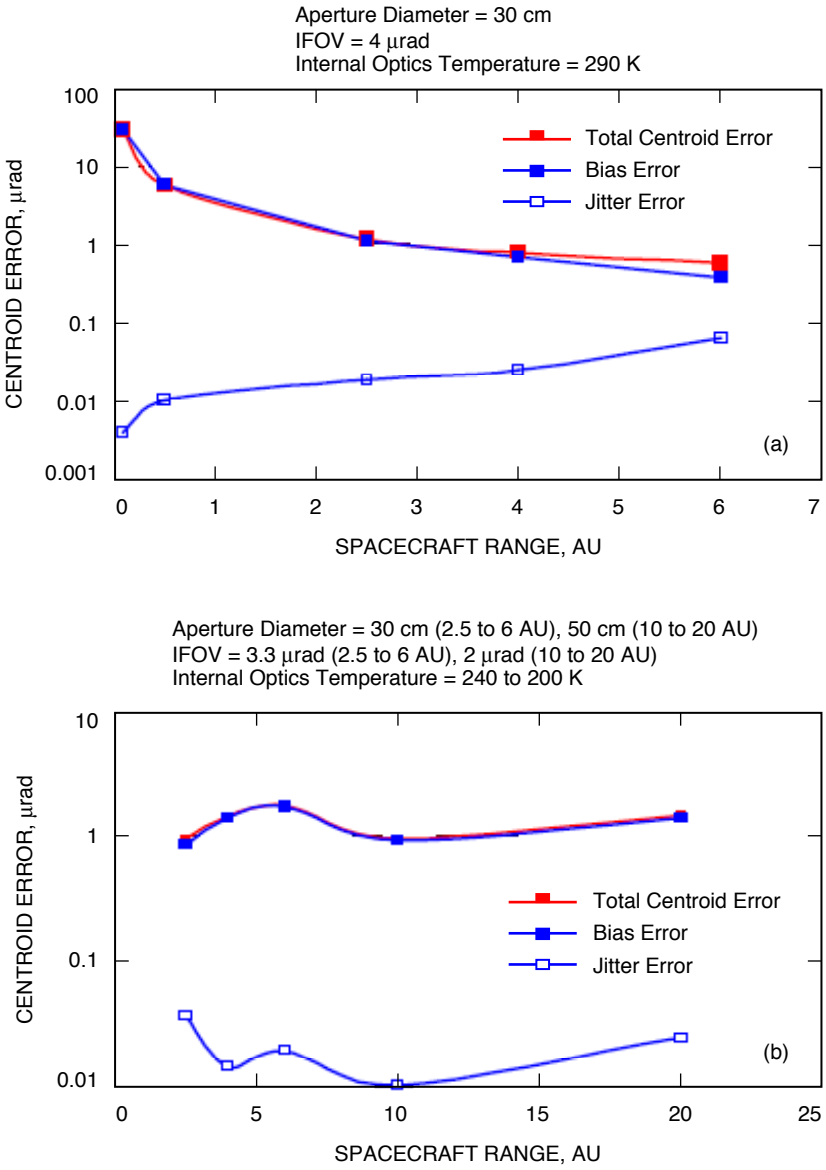

Fig. 16. Summary of the centroiding analysis performed on nonuniform emissivity Earth images with (a) a narrowband QWIP (8 to 9 μm) FPA and (b) a broadband QWIP (8 to 13 μm) FPA.

In order to deliver the communication beam to the receiver telescope, the deep-space optical communication transceiver (OCT) adds a point-ahead correction. This term will be the vector sum of the angular component due to cross-velocity between the spacecraft and the receiver and the angular offset between the ground-based Earth receiver and the geometrical center of Earth. Figure 17 graphically describes the vectors that make up the total point-ahead angle. The view of the figure is as seen by the LWIR Earth tracker focal-plane array. The offset vector is determined using Earth local time.

In order to precisely determine the fixed offset angular component, the spacecraft must have knowledge of Earth time. Current mission operations do not require knowledge of Earth time at the spacecraft. Spacecraft activity is based on the local master clock (i.e., a crystal oscillator). Older missions (e.g., Voyager, Cassini) would let the clock run freely, and the ground system (i.e., Deep Space Network) would compensate for drifts and corrections. A few recent missions (e.g., Mars Odyssey) have active updates

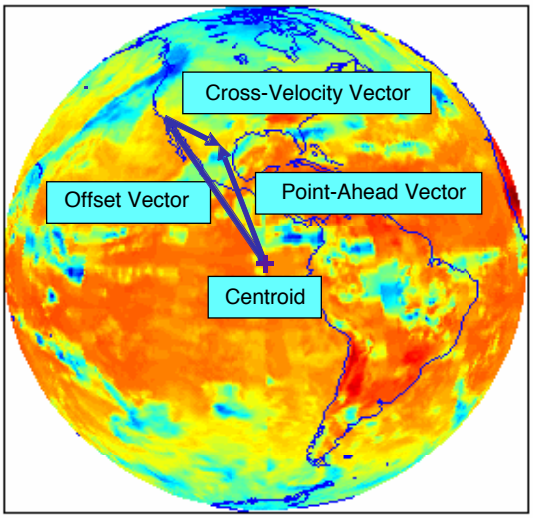

Fig. 17. Earth LWIR tracker graphical representation of the reference frame. The center of Earth (centroid) is determined by centroiding routines on the image. The offset vector to the receiver is computed based on Earth time. The color code indicates the different temperatures of the Earth image.

to "reset" the spacecraft clock, correcting for drifts. Time correlation packets are sent from the ground to the spacecraft for synchronization. The resolution of the spacecraft clock depends on the needs of the mission. Currently there are two classes generally used: (1) 1 to 10 s and (2) 1 to 100 ms.

The point-ahead angle due to two-way light time, $\Theta_{\text{pa.twlt}}$, for an LWIR pointing architecture is determined by the transverse relative cross-velocity between the transmitter, T (see Fig. 18), at the spacecraft and the receiver at Earth, R. This term includes the spacecraft motion, the Earth's orbital motion, and the Earth's rotation. The angular separation as seen from the spacecraft is denoted by $\Theta_{\text{pa.offset}}$:

$$\begin{aligned} \Theta_{\text{pa}} &= \Theta_{\text{pa.twlt}} + \Theta_{\text{pa.offset}} \\ \Theta_{\text{pa.twlt}} &= \frac{2v}{c} \end{aligned} \tag{43}$$

The accuracy of the transformation of the spacecraft clock to Earth time depends on the ground system and the clock references used. Transformations to the sub-second level are routinely done today. The DSN timing system currently is being upgraded from its original 30-year system, and millisecond-level accuracy has been achieved with the new DSN timing and clocks [17].[3] Using this transformation and predicts, it should be possible to know Earth time at the spacecraft with a precision in the 1- to 1000-ms range, mainly driven by the spacecraft clock accuracy.

To estimate the pointing-accuracy error due to the accuracy of the Earth time, consider the one-dimensional case as illustrated in Fig. 19. Assuming that the receiver is at the equator and rotation is at a constant rate, the point-ahead angle contribution from the offset can be determined in terms of the Earth geometry, and referencing the angles relative to the centroid position gives the following expression:

[3] T. Brady, personal communication, Autonomy and Control Section, Jet Propulsion Laboratory, Pasadena, California, May 23, 2006.

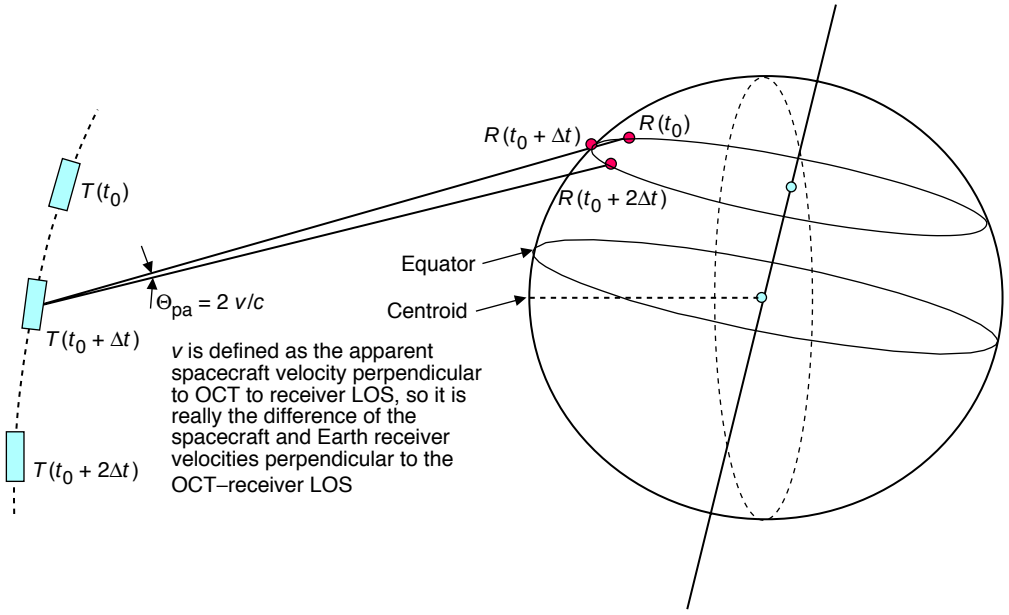

Fig. 18. Point-ahead angle geometry in the LWIR acquisition, tracking, and pointing (ATP) pointing architecture.

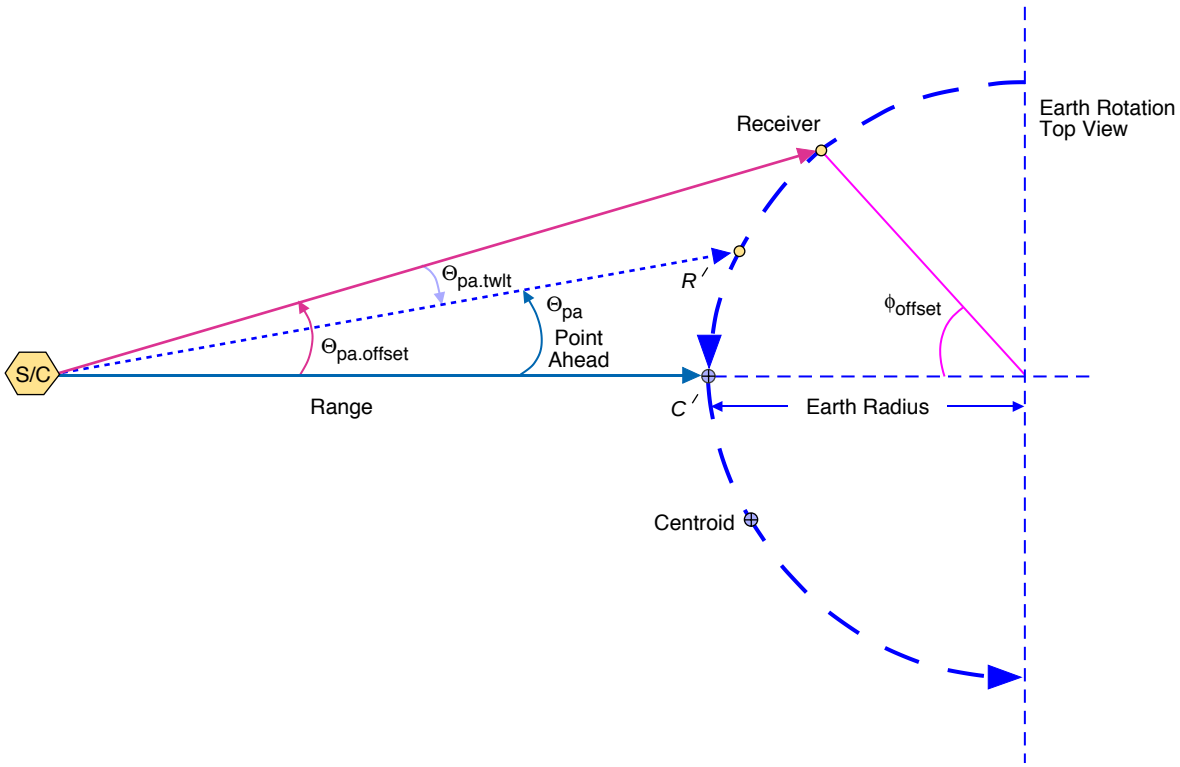

Fig. 19. One-dimensional illustration of the point-ahead geometry from a deep-space spacecraft to an Earth-based receiver. The dashed arrow represents Earth rotation along the equator.

$$\Theta_{\text{pa.offset}} = \frac{\text{Re}\sin(\phi_{\text{offset}})}{\text{range}} = \frac{\text{Re}\sin(\phi_{\text{offset}})}{c\Delta T} \tag{44}$$

where Re is the Earth radius, c is the velocity of light, and ΔT is the one-way light-time. To determine the offset angle, ϕ_{offset}, the local Earth time, T_e, is required:

$$\phi_{\text{offset}} = (T_{\text{offset}} + T_e)\frac{2\pi}{T_{\text{rot}}} \tag{45}$$

where T_{rot} represents Earth rotation period, T_{offset} is the calibration time offset at acquisition, and T_e is Earth receiver local time at the spacecraft. Combining Eq. (45) with Eq. (44) shows that the dependence on Earth time is

$$\Theta_{\text{pa.offset}} = \frac{\text{Re}}{c\Delta T}\sin\left[\frac{2\pi}{T_{\text{rot}}}(T_{\text{offset}} + T_e)\right] \tag{46}$$

To obtain the error dependence, the partial derivative of the point-ahead angle with respect to the Earth time is taken,

$$\partial\Theta_{\text{pa}} = \frac{\text{Re}}{c\Delta T}\cos\left[\frac{2\pi}{T_{\text{rot}}}(T_{\text{offset}} + T_e)\right]\frac{2\pi}{T_{\text{rot}}} * \partial T_e \tag{47}$$

This error function is plotted in Fig. 20 as a function of range for four cases of Earth time uncertainty, ranging from 1 ms to 1 s. It is observed that for ranges greater than 0.5 AU and with a time uncertainty better than 1 s the error contribution to the pointing accuracy is less than 6 nrad.

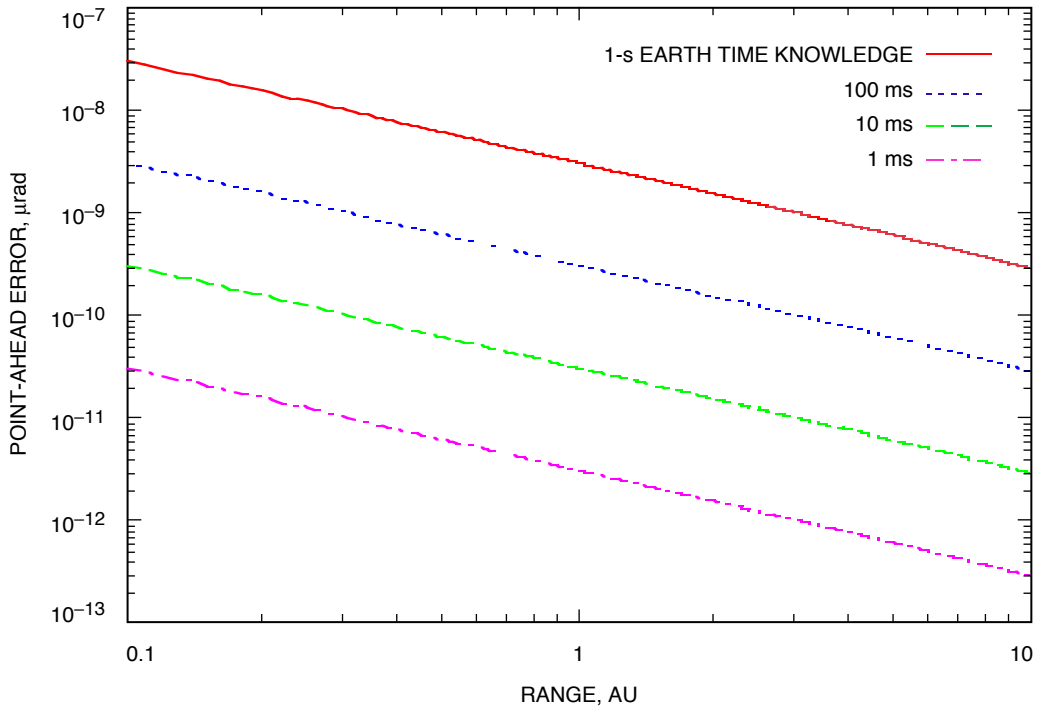

Fig. 20. Point-ahead error as a function of range for various Earth time accuracies.

V. Conclusion

In this article, a preliminary analysis of the prospects and consequences of utilizing the LWIR Earth image as an absolute pointing reference were addressed. A simplified concept of operations would result whereby implementing optical communications from the farthest reaches of the solar system would be eased. On the other hand, several issues that probably will need further analysis and evaluation have been identified, although none of them appears to be insurmountable. Foremost among these is the need for an image processing approach whereby the bias shown to occur due to the nonuniform emissivity can be reduced. Future studies will focus on utilizing additional information about the Earth image, for example, its shape, to correct the offset error. Other issues relate to identifying materials that can be used for an optical system that must transmit at near-infrared and LWIR wavelengths. We have not researched these materials issues extensively; nor have we identified a provisional solution. The need for cold optics in order to prevent excessive background levels will introduce new methods of testing optics on the ground prior to launch, as well as involve novel strategies for maintaining cold optics during flight. The latter may actually save thermal control resources but needs to be evaluated more thoroughly. Finally, this scheme would require the spacecraft to have fairly accurate knowledge of Earth time (within 1 s) in order to determine the location of the ground receiver from a sufficiently accurate determination of the Earth geometric center. This also introduces new operational considerations since current spacecraft from deep space do not need this knowledge and all timing offsets are done with ground processing.

References

[1] W. D. Williams, M. Collins, D. M. Boroson, J. Lesh, A. Biswas, R. Orr, L. Schuchman, and O. S. Sands, "RF and Optical Communications: A Comparison of High Data Rate Returns from Deep Space in the 2020 Timeframe," *Proceeding of the 12th Ka and Broadband Communications Conference*, Naples, Italy, September 2006, in press.

[2] S. Lee, G. G. Ortiz, W. T. Roberts, and J. W. Alexander, "Feasibility Study on Acquisition, Tracking, and Pointing Using Earth Thermal Images for Deep-Space Ka-Band and Optical Communications," *The Interplanetary Network Progress Report 42-155, July–September 2003*, Jet Propulsion Laboratory, Pasadena, California, pp. 1–18, November 15, 2003.
http://ipnpr/progress_report/42-155/155E.pdf

[3] H. Hemmati, Y. Chen, S. Lee, and G. G. Ortiz, "Earth-Image Tracking in the IR For Deep-Space Optical Communications," *2005 Digest of the LEOS Summer Topical Meetings*, San Diego, California, TuA1.1, pp. 27–28, July 25–27, 2005.

[4] J. J. Scozzafava, D. M. Boroson, R. S. Bondurant, A. D. Pillsbury, J. W. Burnside, N. W. Spellmeyer, P. L. Ward, F. K. Knight, M. L. Stevens, and D. R. Bold, "The Mars Lasercom Terminal," *2005 Digest of the LEOS Summer Topical Meetings*, San Diego, California, MA1.2, pp. 9–10, July 25–26, 2005.

[5] C. Chen, J. W. Alexander, H. Hemmati, S. Monacos, T. Yan, S. Lee, J. R. Lesh, and S. Zingales, "System Requirements for a Deep Space Optical Transceiver," *Proceedings of the SPIE, Free-Space Laser Communication Technologies XI*, vol. 3615, pp. 142–152, 1999.

[6] G. G. Ortiz and S. Lee, "Star Tracker Based ATP System Conceptual Design and Pointing Accuracy Estimation," *Proceedings of the SPIE, Free-Space Laser Communication Technologies XVII*, vol. 6105, pp. 6105D-1–6105D-10, 2006.

[7] V. W. S. Chan, "Optical Space Communications," *IEEE Journal On Selected Topics in Quantum Electronics*, vol. 6, pp. 959–975, 2000.

[8] J. E. Harvey, *Light-Scattering Characteristics of Optical Surfaces*, Ph.D. dissertation, University of Arizona, Tucson, Arizona, 1976.

[9] P. R. Spyak and W. L. Wolfe, "Scatter from Particulate-Contaminated Mirrors," *Optical Engineering*, vol. 31, no. 8, p. 1746, August 1992.

[10] *Product Cleanliness Levels and Contamination Control Program*, IEST-STD-CC1246D, Institute of Environmental Sciences and Technology, Rolling Meadows, Illinois, 2002.

[11] M. G. Dittman, "Contamination Scatter Functions for Stray Light Analysis," *Proceedings of the SPIE*, vol. 4774, p. 99, 2002.

[12] A. W. Greynolds, "Formulas for Estimating Stray-Radiation Level in Well-Baffled Optical Systems," *Proceedings of the SPIE*, vol. 257, p. 39, 1980.

[13] M. Born and E. Wolf, *Principles of Optics*, 7th ed., Cambridge: Cambridge University Press, pp. 476–484 and 499–503, 1999.

[14] K. A. Winick, "Cramer-Rao Lower Bounds on the Performance of Charge-Coupled-Device Optical Position Estimators," *J. Opt. Soc. Am. A*, vol. 3, no. 11, p. 1809, 1986.

[15] C.-C. Chen, "Effect of Earth Albedo Variation on the Performance of a Spatial Acquisition Subsystem Aboard a Planetary Spacecraft," *The Telecommunications and Data Acquisition Progress Report 42-95, July–September 1988*, Jet Propulsion Laboratory, Pasadena, California, pp. 202–211, November 15, 1988. http://ipnpr/progress_report/42-95/95T.PDF

[16] B. Moision, "Bounds on the Error Variance when Estimating the Position of an Image," *The Interplanetary Network Progress Report*, vol. 42-167, Jet Propulsion Laboratory, Pasadena, California, pp. 1–17, November 15, 2006. http://ipnpr/progress_report/42-167/167A.pdf

[17] J. Lauf, M. Calhoun, W. Diener, J. Gonzales, A. Kirk, P. Kuhnle, B. Tucker, C. Kirby, and R. Tjoelker, "Clocks and Timing in the NASA Deep Space Network," *Proceedings of the 2005 IEEE International Frequency Control Symposium and Exposition*, IEEE, Vancouver, British Columbia, Canada, pp. 830–835, August 29–31, 2005.